

# Production of very-high- $n$ strontium Rydberg atoms

S. Ye, X. Zhang, T. C. Killian, and F. B. Dunning

*Department of Physics and Astronomy and the Rice Quantum Institute,  
Rice University, Houston, TX 77005-1892, USA*

M. Hiller<sup>1,2</sup>, S. Yoshida<sup>1</sup>, S. Nagele<sup>1</sup>, and J. Burgdörfer<sup>1</sup>

<sup>1</sup> *Institute for Theoretical Physics, Vienna*

*University of Technology, Vienna, Austria, EU and*

<sup>2</sup> *Physikalisches Institut, Albert-Ludwigs-Universität Freiburg, Freiburg, Germany, EU*

## Abstract

The production of very-high- $n$ ,  $n \sim 300$ -500, strontium Rydberg atoms is explored using a crossed laser-atom beam geometry.  $n^1S_0$  and  $n^1D_2$  states are created by two-photon excitation via the  $5s5p\ ^1P_1$  intermediate state using radiation with wavelengths of  $\sim 461$  and  $\sim 413$  nm. Rydberg atom densities as high as  $\sim 3 \times 10^5\text{ cm}^{-3}$  have been achieved, sufficient that Rydberg-Rydberg interactions can become important. The isotope shifts in the Rydberg series limits are determined by tuning the 461 nm light to preferentially excite the different strontium isotopes. Photoexcitation in the presence of an applied electric field is examined. The initially quadratic Stark shift of the  $n^1P_1$  and  $n^1D_2$  states becomes near-linear at higher fields and the possible use of  $n^1D_2$  states to create strongly-polarized, quasi-one-dimensional electronic states in strontium is discussed. The data are analyzed with the aid of a two-active-electron (TAE) approximation. The two-electron Hamiltonian, within which the  $\text{Sr}^{2+}$  core is represented by a semi-empirical potential, is numerically diagonalized allowing calculation of the energies of high- $n$  Rydberg states and their photoexcitation probabilities.

PACS numbers: 32.80.Rm, 32.60.+i

## I. INTRODUCTION

Studies of alkali atoms in states with large principal quantum numbers  $n$ ,  $n \geq 300$ , have demonstrated the remarkable precision with which atomic Rydberg states can be controlled and manipulated using one, or more, electric field pulses, and have provided a wealth of new insights into the dynamics of chaotic systems and into physics in the ultra-fast ultra-intense regime [1–3]. These studies, however, have been limited to singly-excited electronic states by the difficulty of exciting a second electron in the closed-shell core ion. This restriction can be removed by use of alkaline-earth atoms which have two valence electrons because, following excitation of one electron to a high- $n$  state, the presence of the second valence electron leaves a readily-excited optically-active core ion. For low (total) angular momentum (low- $L$ ) Rydberg states, excitation of the core ion leads to rapid autoionization through electron-electron scattering [4, 5]. As  $L$  increases the autoionization rate decreases and this decrease can serve as a probe of the evolution of the Rydberg electron towards high- $L$  states. For sufficiently high  $L$  the core ion behaves as an independent, essentially-free particle allowing it (and the Rydberg atom) to be manipulated through optical trapping or imaged through laser-induced fluorescence [6]. The autoionization process has been studied by colliding two radially localized electronic wave packets in barium revealing violent rather than gradual energy transfer between the two electrons [7]. Furthermore, the presence of the second valence electron also admits the possibility of creating two quasi-stable two-electron excited states in the planetary atom [8] or frozen planet configurations [9–11]. By taking advantage of the different energy-level structure of singlet and triplet excited states, attractive *and* repulsive inter-atomic interactions in ensembles of Rydberg atoms can be realized using the same element [12]. The goal of our ongoing experimental and theoretical efforts is thus to explore the opportunities that strontium provides to probe new aspects of Rydberg atom physics related to two-electron excited states created either within a single atom or by forming pairs of strongly-coupled Rydberg atoms with well-defined interatomic separation. Central to these studies is the production of very-high- $n$  states as these can be readily manipulated using pulsed electric fields [1] and have extraordinarily strong long-range interactions. With these applications in mind we examine here the creation of  $n \sim 300$ –500 strontium Rydberg atoms via two-photon excitation from the ground state using a crossed atom-laser beam geometry. In the first part of this study, we explore the creation

of strontium  $n^1S_0$  and  $n^1D_2$  Rydberg states. Large photoexcitation rates are achieved that permit creation of multiple Rydberg atoms with internuclear separations approaching those at which Rydberg-Rydberg interactions become important. This opens up the opportunity to study strongly-coupled Rydberg-Rydberg systems under carefully controlled conditions. As a test of the spectroscopic resolution achievable we obtain the isotope shifts in the series limits for the different strontium isotopes present in the beam. Another focus is on photoexcitation in a dc electric field. The character of the optically accessible Rydberg states changes markedly as the strength of the applied field is increased. We examine these changes and discuss the possibilities for generation of strongly polarized states, which form the basis of many of the protocols used to engineer Rydberg wave packets. The results are analyzed with the help of a two-active-electron (TAE) model that employs numerically exact diagonalization of the two-electron Hamiltonian containing an empirical potential representing the  $Sr^{2+}$  core. Exploiting the  $n$  scaling for Rydberg states allows the comparison of converged numerical results obtained near  $n = 50$  to data recorded experimentally for  $n \gtrsim 300$ .

## II. EXPERIMENTAL APPROACH

The experimental apparatus is shown in Fig. 1. Strontium atoms contained in a tightly-collimated beam are excited to the desired high- $n$  (singlet) state using the crossed outputs of two frequency-doubled diode laser systems. The first “blue” 461 nm laser is tuned to the  $5s^2\ ^1S_0 \rightarrow 5s5p\ ^1P_1$  transition while the second “purple” 413 nm laser drives the transition from the intermediate  $5s5p\ ^1P_1$  state to the target state (this two-photon scheme is shown in the inset of Fig. 1). When crossing the atom beam, the linearly polarized laser beams travel in opposite directions. By means of half-wave plates, their polarization vectors can be aligned with either the  $x$ - or  $z$ -axis. We explore excitation with both collinear ( $z$ - $z$ ) as well as orthogonal ( $x$ - $z$ ) laser polarizations. Since the two wavelengths are comparable, the use of counter-propagating light beams can largely cancel Doppler effects associated with atom beam divergence resulting in narrow effective experimental line widths. The strontium atom beam is provided by an oven that can operate at temperatures of up to 680°C and which can, with appropriate collimation, provide a  $\sim 1$ mm-diameter beam with a full width at half maximum divergence of  $\sim 4$  mrad at densities approaching  $10^9\text{ cm}^{-3}$ . As described

elsewhere [13], residual stray fields in the experimental volume are reduced to  $\leq 50\mu\text{Vcm}^{-1}$  by application of small offset potentials to the electrodes that surround it.

Measurements are conducted in a pulsed mode. The output of the 461 nm laser is chopped into a series of pulses of  $\sim 0.5\ \mu\text{s}$  duration and 20 kHz pulse repetition frequency using an acousto-optical modulator. The laser is unfocused and has a diameter of  $\sim 3\ \text{mm}$ . Its intensity,  $\sim 10\ \text{mW cm}^{-2}$ , was selected to limit line shifts and broadening due to effects such as the ac Stark shift and Autler-Townes splitting [14]. Its pulse width,  $\sim 0.5\ \mu\text{s}$ , is chosen because for shorter pulse durations the widths of the spectral features become increasingly transform limited. The 413 nm laser remains on at all times and its beam is focused to a spot with a full width at half maximum (FWHM) diameter of  $\sim 170\ \mu\text{m}$ , resulting in an intensity of  $\sim 250\ \text{W cm}^{-2}$ . The frequencies of both lasers are stabilized and controlled with the aid of an optical transfer cavity locked to a polarization-stabilized HeNe laser. This cavity allows uninterrupted tuning of the lasers over frequency ranges of up to  $\sim 800\ \text{MHz}$ . Following each laser pulse, the probability that a Rydberg atom is created is determined by state-selective field ionization for which purpose a slowly-rising (risetime  $\sim 1\ \mu\text{s}$ ) electric field is generated in the experimental volume by applying a positive voltage ramp to the lower electrode. Product electrons are accelerated out of the interaction region and are detected by a particle multiplier. Because only one output pulse from the multiplier can be detected following each laser pulse in the present setup, the probability that a Rydberg atom is created during any laser pulse is maintained below  $\sim 0.4$  to limit saturation effects. This can be accomplished by reducing the strontium atom beam density by operating the oven at a lower temperature ( $\sim 500^\circ\text{C}$ ), and/or by reducing the 413 nm laser power using a neutral density filter.

### III. TWO-ACTIVE-ELECTRON MODEL

#### A. Model Hamiltonian

While alkali atoms are well described by single-active electron models, the same does not hold for alkaline-earth atoms which, in addition to the closed-shell configuration of core electrons, possess two valence electrons. We analyze the excitation spectra for strontium by

means of a two-active-electron (TAE) model. The Hamiltonian reads

$$H = \frac{p_1^2}{2} + \frac{p_2^2}{2} + V_{\ell_1}(r_1) + V_{\ell_2}(r_2) + \frac{1}{|\vec{r}_1 - \vec{r}_2|}, \quad (1)$$

where  $V_{\ell_i}(r_i)$  is an angular-momentum dependent semi-empirical model potential [15] representing the  $\text{Sr}^{2+}$  ion. The latter includes a core polarization correction and is of the form

$$V_{\ell}(r) = -\frac{1}{r} [2 + 36 \exp(-\alpha_1^{\ell} r) + \alpha_2^{\ell} r \exp(-\alpha_3^{\ell} r)] - \frac{\alpha_{\text{cp}}}{2r^4} [1 - \exp[-(r/r_c^{\ell})^6]] , \quad (2)$$

where the parameters,  $\alpha_i^{\ell}, r_c^{\ell}$ , are obtained by fitting to known energy levels of the  $\text{Sr}^{+}$  ion and the experimental core polarizability  $\alpha_{\text{cp}} = 7.5$  is  $\ell$ -independent [15]. (Atomic units are used throughout, unless otherwise stated.) Fine-structure (FS) corrections are neglected as the preliminary calculations including FS corrections show that they are of minor importance for very high  $n$ . The atomic eigenenergies and eigenstates are obtained by numerical diagonalization of the Hamiltonian (Eq. 1). First, the single-particle orbitals  $|\phi_{n_i, \ell_i, m_i}\rangle$  and orbital energies  $E_{n_i, \ell_i, m_i}$  for the  $\text{Sr}^{+}$  ion with

$$H_{\text{ion}} = \frac{p^2}{2} + V_{\ell}(r) \quad (3)$$

are generated using the generalized pseudo-spectral method [16]. This method can efficiently describe wave functions on both long and short length scales by using a non-uniform spatial grid optimized for the potential employed. When FS corrections are included, the orbital energies agree well with the measured values [17, 18]. Whereas spin-orbit coupling is neglected (Eq. 3), the calculated energies do agree with the spin-averaged measured values [15]. However, measured energy levels for the ionic p-states are available only for  $n_i \leq 8$  which introduces uncertainty in the the model potential parameters. Using these one-electron orbitals the basis states of the two-electron Hamiltonian (Eq. 1) are constructed as

$$|n_1 \ell_1 n_2 \ell_2; LM\rangle = \sum_{m_1+m_2=M} \frac{1}{\sqrt{2}} \left[ C(\ell_1, m_1; \ell_2, m_2; L, M) |\phi_{n_1, \ell_1, m_1}\rangle |\phi_{n_2, \ell_2, m_2}\rangle \right. \\ \left. \pm (-1)^{\ell_1+\ell_2+L} C(\ell_2, m_2; \ell_1, m_1; L, M) |\phi_{n_2, \ell_2, m_2}\rangle |\phi_{n_1, \ell_1, m_1}\rangle \right], \quad (4)$$

where  $L$  is the total angular momentum,  $M$  is its projection onto the quantization axis, and the Clebsch-Gordan coefficients are given in terms of 3j symbols as

$$C(\ell_1, m_1; \ell_2, m_2; L, M) = (-1)^{-\ell_1+\ell_2-M} \sqrt{2L+1} \\ \times \begin{pmatrix} \ell_1 & \ell_2 & L \\ m_1 & m_2 & -M \end{pmatrix}. \quad (5)$$

The  $\pm$  sign in Eq. (4) distinguishes basis states symmetric (antisymmetric) with respect to electron exchange in coordinate space representing the singlet (triplet) sector. In order to obtain the spectrum in the presence of a dc electric field oriented along the  $z$ -axis, the Hamiltonian  $H(F) = H + F(\hat{z}_1 + \hat{z}_2)$  with the two-electron dipole operator  $\hat{z}_1 + \hat{z}_2$  is diagonalized, yielding the desired eigenvalues and eigenstates.

Since the principal quantum numbers  $n_1, n_2$  of the orbitals describe the excited states of the  $\text{Sr}^+$  ion and not those of neutral strontium, the quantum number  $n$  of the Rydberg atom associated with the calculated eigenstates of the two interacting electrons

$$|nLM\rangle = \sum_{n_1, \ell_1} \sum_{n_2, \ell_2} c_{n_1, n_2, \ell_1, \ell_2} |n_1 \ell_1 n_2 \ell_2; LM\rangle. \quad (6)$$

is assigned in agreement with known excitation series taking into account perturber states. This is not always straightforward as a few states are hard to identify. For example, the spectroscopic literature [18] lists a 4d5p state in the  $^1\text{P}_1$  sector while, in agreement with [19], our calculations reveal no state with dominant 4d5p character clearly pointing to a strong departure from an independent-particle description.

In the present work, our interest centers on the spectrum of high- $n$  strontium Rydberg states associated with excitation of a single electron. While a few perturber states are important in the low  $n$  regime, the high- $n$  spectrum remains largely unaffected. The quantum numbers  $(n_1, \ell_1)$  of the outer Rydberg electron extend over a wide range; however, those  $(n_2, \ell_2)$  of the inner electron are dominated by a limited number of low-lying states. We can thus truncate the expansion in terms of orbitals of the inner electron to these dominant orbitals which greatly facilitates the numerical diagonalization. More precisely, all numerical results presented here employ six inner electron  $n\ell$  orbitals (5s, 4d, 5p, 6s, 5d, and 6p). For a fixed component,  $M = 0$ , and an excited state with principal quantum number  $n = 50$ , the total Hamiltonian has a dimension of about 40 000. At vanishing electrical field, the latter consists of *uncoupled* blocks of constant total angular momentum  $L$ . However, for excitation in a dc electric field as considered below, the relevant energy in the vicinity of the target level is identified and the resulting Stark matrix to be diagonalized can have a dimension as low as 1 000, rendering our truncated-basis approach numerically inexpensive. Convergence is checked by increasing the number of inner electron orbitals until the relative error in the eigenenergies compared with the results using 14 inner electron orbitals is below 0.1%. For high  $n$  states below the first ionization threshold the present configuration-interaction

method should provide accuracies that are at least comparable to, if not even higher than, R-matrix methods which solve the eigenproblem within a reaction volume of finite radius  $r_0$ , the latter being determined by the largest extent of the inner electron configurations.

## B. Scaling

Since quantum calculations of spectra and transition probabilities for  $n \gtrsim 300$  using the present TAE model are not tractable, we employ scaling relations to extrapolate our converged numerical results for the range  $10 \lesssim n \lesssim 50$  to very high  $n$ . As a starting point, we employ the well-known classical scaling relations for the Rydberg states in a pure Coulomb potential:

for energies,

$$\frac{E_n}{E_{n_0}} = \left(\frac{n_0}{n}\right)^2, \quad (7a)$$

for electric field strength,

$$\frac{F_n}{F_{n_0}} = \left(\frac{n_0}{n}\right)^4, \quad (7b)$$

for dipole moment,

$$\frac{d_n}{d_{n_0}} = \left(\frac{n}{n_0}\right)^2, \quad (7c)$$

for transition matrix elements from low-lying states  $i$  to Rydberg states,

$$\frac{d_{i,n}}{d_{i,n_0}} = \left(\frac{n_0}{n}\right)^{3/2}, \quad (7d)$$

and for the critical fields,  $F_{\text{cross},n} \simeq 1/(3n^5)$ , at which states in adjacent  $n$  manifolds first cross

$$\frac{F_{\text{cross},n}}{F_{\text{cross},n_0}} = \left(\frac{n_0}{n}\right)^5. \quad (7e)$$

In the presence of the  $\text{Sr}^{2+}$  core and the additional valence electron, the scaling in  $n$  [Eq. (7)] can be extended to the effective quantum number

$$n^* = n + \delta_\ell + \beta_\ell E_n \quad (8)$$

of the Rydberg-Ritz formula [20]. In Eq. (8),  $\delta_\ell$  is the  $n$  independent but  $\ell$  dependent quantum defect while the  $n$  (or energy) dependent correction is given by the Ritz coefficient,  $\beta_\ell$ . Our strategy is now to determine  $\beta_\ell$  and  $\delta_\ell$  by diagonalizing the model Hamiltonian Eq. (1) in the basis [Eq. (6)] truncated at  $n = 85$ . From the resulting series of energy

eigenvalues and transition matrix elements ( $n \gtrsim 20$ ), we can, provided they are free from the influence of perturber states, extrapolate to very high  $n$  employing the scaling relationships [Eq. (7)] and the effective quantum numbers  $n^*$ .

## IV. ZERO-FIELD PHOTOEXCITATION

### A. Quantum defects

As a first test of the TAE model we compare (see Fig. 2) the energies of low- $L$  and intermediate  $n$  Rydberg states, expressed in terms of  $n$ -dependent quantum defects,  $\mu(n) = n - n^*$ , [Eq. (8)] with experimental data [12, 21–23]. Overall, our TAE energy values agree well with the experimental data as do the results of multichannel quantum defect theory [22] and of R-matrix calculations [15] which employ the same semi-empirical model potential. However, a small discrepancy between theory and experiment is seen for the quantum defects of the P and D states, i.e., the calculated values slightly underestimate the measured quantum defects and we return to this in a moment. The effective quantum defects increase with  $n$ , especially for D states yielding a non-vanishing Ritz coefficient  $\beta_2 \simeq -43$ . The value for P states,  $\beta_1 \simeq -8$ , is significantly smaller while the coefficient for S states  $\beta_0 \simeq 0.08$  is close to zero. In the series limit, the calculated values of the  $n$ -independent quantum defects  $\delta_0 = 3.26$ ,  $\delta_1 = 2.65$  and  $\delta_2 = 2.33$  are slightly lower than the measured values  $\delta_0 = 3.26$ ,  $\delta_1 = 2.71$  and  $\delta_2 = 2.38$ . For lower  $n$ ,  $\mu(n)$  deviates strongly from simple single-electron Coulomb scaling signaling the presence of perturber states in the two-electron system. These deviations are, however, of negligible importance for the high- $n$  limit of interest here. Adjusting the model-potential parameters and/or including dielectric core polarization terms [24] yields nearly identical results, still underestimating the measured quantum defects. This is due to the fact that, for all model potentials employed, the calculated energy levels of the  $\text{Sr}^+$  ion exhibit deviations from the measured values which are of the same order of magnitude. The precise estimation of the quantum defect, however, requires accurate values not only of the energy of the excited state but also of the ionization threshold. Thus, small but finite errors in ionic energies are passed on to the energy values of neutral strontium and become non-negligible for high- $n$  levels. Alternatively, it is possible to optimize the model potential in order to minimize these deviations. For the present two-



photon excitation study we chose the model potential of Ref. [15] since the intermediate  $5s5p\ ^1P_1$  state as well as the excited states in the S- and D-sectors are reasonably well represented (see Fig. 2).

## B. Oscillator strengths

A second test of the TAE model is provided by comparing the calculated oscillator strengths with those measured experimentally (see Fig. 3) both for the  $5s^2\ ^1S_0 \rightarrow 5s5p\ ^1P_1$  transition, and for the subsequent transitions to the Rydberg manifolds,  $5s5p\ ^1P_1 \rightarrow 5sns\ ^1S_0$  and  $5snd\ ^1D_2$ . The first transition provides a sensitive test of the limitations of independent-electron models. This transition is strongly influenced by configuration mixing, closely connected to the inclusion of the  $4d5p\ ^1P_1$  configuration among the members of the  $5snp\ ^1P_1$  manifold mentioned previously. The collective, i.e., multi-electron, character of the transition is reflected in an oscillator strength exceeding unity. The value from our TAE model  $f_{5s5p} = 2.02$  agrees with the experimental value  $f_{5s5p}^{\text{expt}} = 1.91$  and is in reasonable agreement with the calculations by Vaeck et al. [19] and Werij et al. [25]. The subsequent  $5s5p\ ^1P_1 \rightarrow 5sns\ ^1S_0$  or  $5snd\ ^1D_2$  transitions control the excitation of the Rydberg manifolds of interest here and allow for a test of  $n$ -scaling of the oscillator strengths and transition probabilities. For low  $n$  ( $n \leq 20$ ) significant deviations from simple Coulomb  $n$  scaling [Eq. (7c)] are observed. Most prominent is the Cooper minimum near  $n = 13$  ( $n^* = 10$ ) in the excitation probability to the  $^1D_2$  states. The observed minimum is associated with a change of sign in the dipole matrix elements. To our knowledge, this Cooper minimum has not been reported in the literature. We note that the vanishing dipole coupling in the vicinity of the Cooper minimum increases the influence of otherwise weak effects, such as spin-orbit interactions. The latter are, of course, not captured by our non-relativistic Hamiltonian [Eq. (1)]. Experimental data [22] indicate that at  $n \approx 15$  the singlet and triplet  $L = 2$  Rydberg series of strontium undergo an avoided crossing, i.e.,  $L$ - $S$  coupling breaks down. Our calculations agree well with the calculations by Werij et al [25] for  $n^* < 8$  but underestimate the spectroscopic data for higher  $n$  ( $20 \leq n \leq 68$ ) [26]. The oscillator strength smoothly approaches the  $(n^*)^{-3}$  scaling from below. To further check the validity of our calculations, the dipole matrix elements for  $\langle 5s5p^1P_1 | z | 5sns^1S_0 \rangle$  (Fig. 3b) and  $\langle 5s^2\ ^1S_0 | z | 5snp^1P_1 \rangle$  (Fig. 3c) transitions are compared with available data. Our calculations

agree reasonably well with the results of earlier calculations [25] for the former (Fig. 3b), and the measurements [27, 28] for the latter (Fig. 3c). We note that the dipole matrix elements are evaluated from the oscillator strength,  $f$ , or the transition probability,  $A$ , published in the references mentioned above assuming the relationships  $f = 2\omega|\langle 5snl|z|5sn'l'\rangle|^2$  and  $A = 4\omega^3|\langle 5snl|z|5sn'l'\rangle|^2/(3c^3)$ .

In the following we estimate the production rates for  $5snd$   $^1D_2$  and  $5sns$   $^1S_0$  Rydberg atoms near  $n \simeq 300$ . Fig. 4 illustrates the evolution of the photoexcitation spectrum from  $n = 39$  to 280. The calculated spectra for  $n = 30$  and 50 are compared with spectra measured near  $n = 280$ . The calculated spectrum for  $n = 50$  is convoluted with a Gaussian to match the (scaled) measured experimental line width while for  $n = 30$  a smaller line width is chosen to resolve the S- and D-states (near  $n \simeq 30$  the spacing of the  $(n+1)S$  and  $nD$  features is very small). The width of the measured lines is principally attributed to transit time broadening (the transit time of an atom through the 413 nm laser spot is  $\sim 300$  ns) with smaller contributions from the finite laser pulse width and fluctuations in the laser frequencies during the  $\sim 1$  s accumulation time for each data point in the spectrum. The energy axes in Fig. 4 are scaled as in Eq. (7). The arrows in Fig. 4a show the predictions for the position of the spectral lines based on the Rydberg-Ritz scaling [Eq. (8)] derived from the calculated spectrum for lower  $n$ . While the position of the S-state is well predicted, the D-state position is slightly off due to the underestimated quantum defect [Fig. 2]. The positions of the  $n$   $^1S_0$  states relative to the two adjacent  $n$  manifolds are nearly invariant with respect to  $n$  as the quantum defects of the  $n^1S_0$  states are nearly  $n$ -independent. On the other hand, the relative positions of the  $n$   $^1D_2$  states vary with  $n$  mirroring the  $n$ -dependent quantum defect. The measured relative size of the  $^1D_2$  to  $^1S_0$  lines near  $n = 280$  is  $\sim 8.7$ . For lower  $n$  the calculations indicate a moderate increase of the  $^1D_2/^1S_0$  ratio and – in line with the  $n^*$  scaling – predict a ratio of  $\sim 4$  at  $n = 280$ . The origin of this discrepancy is not yet clear. Experimentally, stray fields might enhance this ratio, as might any deviations from collinear alignment of the polarization axes of the two lasers. As will be discussed below, the measured excitation rate of  $^1D_2$  states is smaller than the theoretical prediction indicating that the enhanced ratio is due to a suppression of  $^1S_0$  state excitation rather than an enhancement of  $^1D_2$  state excitation.

It is instructive to compare the excitation spectrum calculated within the present TAE approximation with the results of a single-active-electron (SAE) model with a model poten-

tial similar to that described in Ref. [29]. We have found that the quantum defects resulting from the SAE model display a very weak  $n$ -dependence. That is, the eigenenergies and the quantum defects can be obtained quite accurately for an optimized model potential but only for a limited range of principal quantum numbers. When adjusting the model parameters to fit the asymptotic quantum defects, the high Rydberg states are reasonably well represented by the SAE model. However, the calculated oscillator strengths fail to reproduce the measured excitation spectra which we trace to an inaccurate description of the  $5s5p$  state. This failure reflects the fact that the first excitation step is strongly influenced by electron-electron interactions not accounted for by the SAE model.

### C. Rydberg excitation rates

For applications involving strongly coupled Rydberg atoms, it is crucial to achieve high excitation densities which poses a challenge given the  $(n^*)^{-3}$  scaling of the oscillator strength. We have therefore measured the strontium Rydberg excitation rates that can be achieved in the beam. Measurements at  $n \sim 310$  show that the probability to create a Rydberg atom at the peak of a  $^1D_2$  feature during a  $\sim 500$  ns laser pulse can be made large. To avoid saturation effects, in the standard setup the probability is purposely maintained below  $\sim 0.4$  by substantially reducing the strontium atom beam density by operating the oven at  $\sim 500$  °C. However, tests undertaken at higher operating temperatures in which the 413 nm laser beam was attenuated using neutral density filters to limit the excitation rate showed that, with the oven operating at  $\sim 630$ °C and using the full 413 nm laser power ( $\sim 70$  mW),  $\sim 15$  Rydberg atoms can be produced per laser pulse which, when allowance is made for the motion of atoms in the beam during the 500 ns-duration laser pulse, corresponds to a product Rydberg atom density of  $\sim 3 \times 10^5$  cm $^{-3}$ .

To a good first approximation, the excitation rate can be estimated by assuming two sequential one-photon processes. The first transition (Rabi period 0.1  $\mu$ s) may be considered as saturated having a Lorentzian profile with a width of  $\sim 10$  MHz. For an intensity of 250 W cm $^{-2}$ , the second transition has a width  $\omega \sim 0.5$  MHz and thus a Rabi period of about 2  $\mu$ s. Given the relatively long atomic transit time,  $t_{\text{transit}} \sim 300$  ns, through the 413 nm laser beam, a linear (Fermi Golden Rule) estimate would likely overestimate the excitation probability. Therefore, this probability is obtained using the Rabi formula

$P(\Delta) = \omega^2(1 - \cos[(\sqrt{\omega^2 + \Delta^2})t_{\text{transit}}])/2(\omega^2 + \Delta^2)$ , where  $\Delta$  is the detuning. If the excitation is considered as an incoherent sequence of two transitions, the total Rydberg excitation probability is given by the integral (over the detuning) of the product of the two Lorentzian excitation profiles. This approach yields an excitation probability of  $\sim 1\%$  per atom. Given the estimated strontium atom beam density of  $\sim 10^8 \text{ cm}^{-3}$  this would suggest creation of Rydberg atom densities of  $\sim 10^6 \text{ cm}^{-3}$  Rydberg atoms per laser pulse which are somewhat higher than the experimental measurements.

Rydberg atom densities of  $\sim 3 \times 10^5 \text{ cm}^{-3}$  result in a typical inter-Rydberg spacing of  $\sim 150 \text{ }\mu\text{m}$  which is approaching distances at which effects due to Rydberg-Rydberg interactions such as blockade become important. Blockade results when the energy level shifts induced by the excitation of a Rydberg atom prevent the excitation of other neighboring atoms. Calculations of such shifts have been undertaken for strontium  $n^1\text{D}_2$  (and other) states for values of  $n$  up to  $\sim 70$  [12]. Extrapolation of these results to  $n \sim 300$  would lead to blockade radii of  $\sim 500 \text{ }\mu\text{m}$  for an effective laser line width of  $\sim 5 \text{ MHz}$ . The validity of this extrapolation to very high  $n$  is, however, an open question. An alternative estimate for the blockade radius can be obtained by considering the dipole-dipole interaction of two permanent dipole moments  $\vec{d}_1, \vec{d}_2, \propto d_1 d_2 / R^3$ , which for extreme high- $n$  parabolic states are of the order of  $\sim n^2 \text{ a.u.}$  This model suggests a blockade radius of  $\sim 150 \text{ }\mu\text{m}$  at  $n \sim 300$ . As an aside we note that the number of Rydberg atoms produced in the present experiments with strontium is much higher than achieved for potassium at comparable beam densities in earlier experiments [1]. This increase is primarily due to a threefold increase in the laser powers available and a factor of three decrease in the effective experimental line width.

#### D. Isotope shifts

As a test of the spectral resolution achievable in the present experimental apparatus we probe the isotope shifts in very high- $n$  Rydberg atoms near the series limit. Fig. 5 shows zero-field excitation spectra recorded in the vicinity of  $n = 282$  for various detunings of the 461 nm laser which were selected to optimize the  $5s^2 \text{ }^1\text{S}_0 \rightarrow 5s5p \text{ }^1\text{P}_1$  transition in the different strontium isotopes. The relative frequencies of these transitions together with other properties of naturally-occurring strontium are listed in Table I [30–32]. In both Table I and Fig. 5, the isotope shifts and hyperfine splittings are quoted relative to the most abundant

$^{88}\text{Sr}$  isotope. The frequency axis in Fig. 5 shows the sum of the 461 nm and 413 nm photon energies.

The reference spectrum obtained with the 461 nm laser tuned to optimally excite the dominant  $^{88}\text{Sr}$  isotope (upper panel) displays a series of sharp peaks associated with the excitation of  $^1\text{D}_2$  and  $^1\text{S}_0$  states (see the spectrum of Fig. 4a). As the 461 nm laser is red detuned from resonance with the  $^1\text{S}_0 \rightarrow ^1\text{P}_1$  transition in  $^{88}\text{Sr}$  (lower panels in Fig. 5), the size of the  $^{88}\text{Sr}$  features in the excitation spectra decrease steadily and new features associated with the excitation of Rydberg states of the other isotopes emerge. Rather easy to identify are the spectral features seen at a detuning of  $\sim -122$  MHz, which optimizes the  $^1\text{S}_0 \rightarrow ^1\text{P}_1$  transition in the  $^{86}\text{Sr}$  isotope. The excitation spectrum is dominated by the creation of  $^{86}\text{Sr}$   $^1\text{D}_2$  states although some residual excitation of  $^{88}\text{Sr}$  isotopes remains. The observed  $^{88}\text{Sr}$ - $^{86}\text{Sr}$  isotope shift in the series limit,  $\sim +210 \pm 5$  MHz, is in agreement with the value obtained by extrapolation of earlier spectroscopic studies at lower  $n$  [33]. Similarly, at a blue laser detuning of  $\sim -273$  MHz which optimizes the  $^1\text{S}_0 \rightarrow ^1\text{P}_1$  transition in the  $^{84}\text{Sr}$  isotope, the excitation of  $^{84}\text{Sr}$   $^1\text{D}_2$  Rydberg states becomes apparent. The observed  $^{88}\text{Sr}$ - $^{84}\text{Sr}$  isotope shift in the series limit,  $+440 \pm 8$  MHz, is again consistent with earlier measurements at lower  $n$  [33]. The fractional abundances of the  $^{86}\text{Sr}$  and  $^{84}\text{Sr}$  isotopes in the beam (see Table I) are directly reflected in the relative intensities of the excitation peaks.

Several features are observed in the excitation spectra at blue laser detunings chosen to favor excitation of the  $^{87}\text{Sr}$  isotope (at detunings of about  $-47$ , and  $-56$  MHz). This (odd) isotope displays strong hyperfine-induced singlet-triplet mixing and strong interactions between states of different  $n$  [34, 35]. A detailed analysis of these features requires stray fields to be reduced to very low levels [34] well beyond the capabilities of the present apparatus.

### E. Extension to higher $n$

We close the discussion of zero-field excitation with Rydberg spectra recorded at even higher values of  $n$  and the 461 nm laser tuned again to the  $^1\text{S}_0 \rightarrow ^1\text{P}_1$  transition in the dominant  $^{88}\text{Sr}$  isotope. It is evident from Fig. 6 that, as  $n$  increases, the number of Rydberg atoms created decreases dramatically as a result of both the decrease in the oscillator strength and the increasing width of the spectral features. For values of  $n \leq 350$ , two well-resolved Rydberg series are seen, corresponding to excitation of  $^1\text{D}_2$  and  $^1\text{S}_0$  states. With

further increases in  $n$  the spectral features begin to broaden significantly, their widths having approximately doubled by  $n \sim 400$ . For even larger values of  $n$  the background signal begins to increase, but a well-resolved Rydberg series is still evident for values of  $n$  up to  $\sim 460$ . For  $n > 500$ , however, it becomes increasingly difficult to discern any Rydberg series. This degradation in the Rydberg spectrum in the limit of very high  $n$  can be attributed to the presence of very small stray background fields in the excitation volume. As discussed below, the effects of such fields become particularly important when they approach the fields at which states in adjacent Stark manifolds cross,  $\sim 50 \mu\text{V cm}^{-1}$  at  $n \sim 500$ . This suggests that stray fields of  $\sim 50 \mu\text{V cm}^{-1}$  remain in the excitation volume which is consistent with earlier estimates of their size.

## V. PHOTOEXCITATION IN A DC FIELD

We focus now on the Stark spectrum for strontium. More specifically, we investigate the spectrum of the singly-excited Rydberg states as a function of the strength  $F_{\text{dc}}$  of a dc field applied along the  $z$  axis. Well-controlled excitation of Stark states is key to creation of ensembles of Rydberg atoms with large permanent dipole moments.

In contrast to the preceding discussion of excitation at vanishing field, we consider orthogonal polarizations of the lasers (experimentally, a half-wave plate was used to rotate the plane of polarization of the 413 nm laser by  $\sim 90^\circ$ ). This leads to excitation of Rydberg states with  $M = \pm 1$  and thus suppresses excitation of  $^1S_0$  states which, in turn, simplifies the excitation spectrum. The calculated Stark spectrum near  $n = 50$  (Fig. 7) illustrates the evolution of the excitation spectrum from the low-field to the high-field regime characterized by the crossing of adjacent manifolds. High- $L$  states, which are nearly degenerate at  $F_{\text{dc}} = 0$ , exhibit linear Stark shifts. States from adjacent Stark manifolds first cross at a field given by Eq. (7e). Initially the low angular momentum  $^1P_1$  and  $^1D_2$  states exhibit only a quadratic Stark effect, a consequence of strong core scattering which prevents the state from acquiring a large dipole moment and limits its polarizability [36]. Exploiting the scaling relations, we display in Fig. 7 the theoretical excitation spectra for field-perturbed  $n^1D_2$  and  $n^1P_1$  states near  $n = 50$  together with the experimental spectra near  $n \simeq 310$ . Fig. 7 also includes the results of previous measurements at  $n = 80$  [4]. In zero field ( $F = 0$ ) only  $n^1D_2$  states can be excited from the intermediate  $5s5p \ ^1P_1$  state. As the strength of the dc field grows,

the  $n^1D_2$  states increasingly couple with other angular momentum states. This increase in  $L$ -mixing results in a marked decrease in the oscillator strengths associated with their excitation. As each “ $n^1D_2$ ” state merges with the linear Stark manifold,  $L$ -mixing is so strong that the effects of core scattering become negligible and the state becomes almost indistinguishable from the nearby extreme (strongly-polarized) Stark states. The small difference in the scaled Stark spectrum between the energy levels calculated (for the “ $52^1D_2$ ”) state and those measured (for the “ $312^1D_2$ ”) state result from the fact that the calculated zero-field quantum defects are somewhat smaller than the experimental values (Fig. 2). These minor quantitative differences aside, the calculated and measured excitation spectra are found to be in good accord.

In view of the close correspondence between measurement near  $n = 310$  and theory near  $n = 50$ , we detail the evolution of the “ $n^1D_2$ ” states with increasing dc field based on the computed energy spectrum at  $n \simeq 50$ . This aims at characterizing the transition from an unpolarized  $n^1D_2$  state to a strongly polarized Stark state. This evolution can be visualized by considering the distribution of projections onto states with parabolic quantum number  $k$

$$\rho(k) = \sum_n \left| {}^H\langle n, k, m | n_{\text{Stark}} \rangle^{\text{Sr}} \right|^2, \quad (9)$$

or, equivalently, the distribution of the  $z$ -component,  $A_z$ , of their Runge-Lenz vectors since  $k$  corresponds to the quantized action of  $-nA_z$ . Here  $|n, k, m\rangle^H$  are the hydrogenic parabolic states and  $|n_{\text{Stark}}\rangle$  describes the numerically exact eigenstate of the singly-excited strontium atom in the dc field. Since the inner valence electron is almost exclusively in the  $5s$  state, i.e.,  $|n_{\text{Stark}}\rangle$  is close to a natural orbital of the two-electron system, the outer-electron state can be factorized to evaluate the overlap. Fig. 8 displays the evolution of the  $k$ -distribution for the “ $52D$ ”  $M = 1$  state as a function of applied field. For weak fields, the  $k$ -distribution is broad covering a wide range of values between  $-n$  and  $n$  indicating that the state is unpolarized. This can be easily understood by recalling that the classical Runge-Lenz vector gives the direction of the major axis of the Kepler ellipse. A wide distribution of  $A_z$  implies an ensemble of Kepler ellipses with  $L = \ell + 1/2$  whose major axes are broadly distributed. For non-hydrogenic atoms that possess a sizable quantum defect, such a distribution results from core scattering which rotates the orientation of the ellipse while maintaining its eccentricity. A minimum in the  $k$ -distribution is seen near  $k = 0$  which mirrors a node of the spherical harmonic  $Y_{\ell=2}^{m=1}$ . As  $F_{\text{dc}}$  is increased this node shifts towards negative  $k$  and the

$k$ -distribution becomes increasingly asymmetric indicating that the state becomes, indeed, gradually polarized. When in the Stark map (see Fig. 7) the state merges with the neighboring Stark manifold, its  $k$ -distribution becomes narrow consistent with evolution towards a narrow range of parabolic states. This is in sharp contrast to the  $k$ -distribution of the “52P” state [Fig. 8] which shows little sign of asymmetry even as the neighboring manifold is approached suggesting that the state is only weakly polarized. The pronounced difference between D and P states arises because P states couple strongly only with adjacent S and D states, both of which are difficult to polarize. The D states, on the other hand, directly couple with neighboring F states which merge with the Stark manifold at relatively small values of  $F_{\text{dc}}$  [see Fig. 8] and become polarized. The sizable polarization of the “52D” state, therefore, results from strong coupling to this polarized “50F” state. In agreement with this line of reasoning, we have found that the  $M = 0$  S state is much less polarized than the  $M = 0$  D state.

We now quantify the degree of polarization in terms of dipole moments,  $\langle z_1 + z_2 \rangle$  [see Fig. 8]. High- $L$  states, nearly degenerate at  $F_{\text{dc}} = 0$ , become polarized even in very weak fields with dipole moments approaching the hydrogenic field-independent value  $\langle (z_1 + z_2) \rangle = (3/2)nk$ . Well-isolated low- $L$  states display a linear response behavior

$$\langle z_1 + z_2 \rangle = -\alpha F_{\text{dc}} \quad (10)$$

with a quadratic Stark shift  $\Delta E = -(1/2)\alpha F_{\text{dc}}^2$ . To lower-order perturbation theory, the atomic polarizability  $\alpha$  is given by

$$\alpha = 2 \sum_{n'} \sum_{L'=L\pm 1} \frac{|\langle nLM | (z_1 + z_2) | n'L'M \rangle|^2}{E_{n'L'M} - E_{nLM}}. \quad (11)$$

Numerical evaluation of Eq. (11) for the 50F state shows that the sum over intermediate states is dominated by a single term, the almost degenerate 50G state. Even in weak fields the resulting large polarizability leads to sizable shifts in energy (see Fig. 7). For the “52P” state coupling to the “52D” state dominates the sum in Eq. (11). However, the large energy difference (see Fig. 7) between these states suppresses large values of  $\alpha$ . The “52D” state lies between the two states “52P” and “50F” to which it is dipole coupled (Fig. 7). The coupling with the “50F” state is dominant leading to polarization on the “downhill” side. As the applied field increases, the growth of the dipole moment becomes non-linear in  $F_{\text{dc}}$  due to the increasing importance of the higher-order perturbation terms, i.e., the strong mixing with



higher  $L$  states. The states can then become strongly polarized and, as seen for the “50F” and “52D” states, their polarizations can approach the limiting value of  $\langle z_1 + z_2 \rangle = 1.5n^2$  a.u.

## VI. CONCLUSIONS

The present work demonstrates that very-high- $n$  strontium Rydberg states with  $n \sim 300$  can be excited with remarkable efficiency by two-photon excitation using a crossed laser-atom beam geometry. Near simultaneous creation of  $\sim 15$  Rydberg atoms within a 500 ns laser pulse is achieved. In fact, for spectroscopy of isolated strontium Rydberg atoms it was necessary to reduce either the beam density or the laser intensity. The photoexcitation spectra recorded in the presence of a dc field suggest it should be possible to create strongly polarized Rydberg states by exciting “ $nD$ ” states in dc fields approaching the crossing field  $F_{\text{cross}}$ . Interpretation of the data was facilitated by a full two-active electron approximation in which the  $\text{Sr}^{2+}$  core is represented by a semi-empirical core potential and which allows the calculation of the excitation spectrum both in the absence and in the presence of a static electric field for Rydberg states with values  $n$  of up to  $n \simeq 50$ . Use of Coulomb scaling including quantum defects and Ritz corrections allows prediction of excitation spectra for very high  $n$  Rydberg states.

The present measurements and simulations suggest that quasi-one dimensional polarized strontium states can be formed at  $n \simeq 300$  that closely resemble extreme parabolic states. Such quasi-one-dimensional states provide a valuable starting point for wave function engineering and can be readily transformed into circular or elliptic wave packets [1]. Wave packet manipulations open up the opportunity to explore the creation of quasi-stable two-electron excited states in which the two electrons are placed in large correlated near-classical orbits that are stabilized by their mutual interactions [8–11]. The capability to create multiple Rydberg atoms during a single laser pulse will allow the study of strongly-coupled Rydberg-Rydberg systems at very high  $n$ . The time evolution of the resulting strongly-correlated wave packet may open up the possibility, through periodic driving, of creating a correlated “molecular” phase-locked Rydberg wave packet.

## Acknowledgments

Research supported by the NSF under Grant No. 0964819, the Robert A. Welch foundation under Grant No. C-0734, and by the FWF (Austria) under grant No. P23359-N16. The Vienna Scientific Cluster was used for the calculations.

- 
- [1] F. B. Dunning, J. J. Mestayer, C. O. Reinhold, S. Yoshida, and J. Burgdörfer, *J. Phys. B* **42**, 022001 (2009).
  - [2] A. Buchleitner, D. Delande, and J. Zakrzewski, *Phys. Rep.* **368**, 409 (2002).
  - [3] R. V. Jensen, S. M. Susskind, and M. M. Sanders, *Phys. Rep.* **201**, 1 (1991).
  - [4] J. Millen, G. Lochead, and M. P. A. Jones, *Phys. Rev. Lett.* **105**, 213004 (2010).
  - [5] W. E. Cooke, T. F. Gallagher, S. A. Edelstein, and R. M. Hill, *Phys. Rev. Lett.* **40**, 178 (1978).
  - [6] P. McQuillen, X. Zhang, T. Strickler, F. B. Dunning, and T. C. Killian, *Phys. Rev. A* **87**, 013407 (2013).
  - [7] S. N. Pisharody and R. R. Jones, *Science* **303**, 813 (2004).
  - [8] M. Kalinski, J. H. Eberly, J. A. West, and C. R. Stroud Jr., *Phys. Rev. A* **67**, 032503 (2003).
  - [9] U. Eichmann, V. Lange, and W. Sandner, *Phys. Rev. Lett.* **64**, 274 (1990).
  - [10] U. Eichmann, V. Lange, and W. Sandner, *Phys. Rev. Lett.* **68**, 21 (1992).
  - [11] K. Richter and D. Wintgen, *Phys. Rev. Lett.* **65**, 1965 (1990).
  - [12] C. L. Vaillant, M. P. A. Jones, and R. M. Potvliege, *J. Phys. B* **45**, 135004 (2012).
  - [13] M. T. Frey, X. Ling, B. G. Lindsay, K. A. Smith, and F. B. Dunning, *Rev. Sci. Instr.* **64**, 3649 (1993).
  - [14] S. H. Autler and C. H. Townes, *Phys. Rev.* **100**, 703 (1955).
  - [15] M. Aymar, C. H. Greene, and E. Luc-Koenig, *Rev. Mod. Phys.* **68**, 1015 (1996).
  - [16] X.-M. Tong and S.-I. Chu, *Chem. Phys.* **217**, 119 (1997).
  - [17] V. Lange, M. Khan, U. Eichmann, and W. Sandner, *Z. Phys. D* **18**, 319 (1991).
  - [18] J. E. Sansonetti, *J. Phys. Chem. Ref. Data* **41**, 013102 (2012).
  - [19] N. Vaeck, M. Godefroid, and J. E. Hansen, *Phys. Rev. A* **38**, 2830 (1988).
  - [20] R. Jastrow, *Phys. Rev.* **73**, 60 (1948).

- [21] J. E. Sansonetti and G. Nave, J. Phys. Chem. Ref. Data **39**, 033103 (2010).
- [22] P. Esherick, Phys. Rev. A **15**, 1920 (1977).
- [23] C. J. Dai, Phys. Rev. A **52**, 4416 (1995).
- [24] E. Luc-Koenig, M. Aymar, J.-M. Lecomte, and A. Lyras, J. Phys. B **31**, 727 (1998).
- [25] H. G. C. Werij, C. H. Greene, C. E. Theodosiou, and A. Gallagher, Phys. Rev. A **46**, 1248 (1992).
- [26] S.-U. Haq, S. Mahmood, M. A. Kalyar, M. Rafiq, R. Ali, and M. A. Baig, Eur. Phys. J. D **44**, 439 (2007).
- [27] W. R. S. Garton, J. P. Connerade, M. A. Baig, J. Hormes, and B. Alexa, J. Phys. B **16**, 389 (1983).
- [28] W. Mende and M. Kock, J. Phys. B **30**, 5401 (1997).
- [29] J. Millen, G. Lohead, G. R. Corbett, R. M. Potvliege, and M. P. A. Jones, J. Phys. B **44**, 184001 (2011).
- [30] R. Beigang, K. Lücke, A. Timmermann, P. West, and D. Frölich, Opt. Comm. **42**, 19 (1982).
- [31] E. Eliel, W. Hogervorst, T. Olsson, and L. Pendrill, Z. Phys. A **311**, 1 (1983).
- [32] S. Mauger, J. Millen, and M. P. A. Jones, J. Phys. B **40**, F319 (2007).
- [33] C. J. Lorenzen, K. Niemax, and L. R. Pendrill, Phys. Rev. A **28**, 2051 (1983).
- [34] R. Beigang, J. Opt. Soc. Am. B **5**, 2423 (1988).
- [35] J.-Q. Sun, K. T. Lu, and R. Beigang, J. Phys. B **22**, 2887 (1989).
- [36] T. P. Hezel, C. E. Burkhardt, M. Ciocca, L. He, and J. J. Leventhal, Am. J. Phys. **60**, 329 (1992).

## Figures

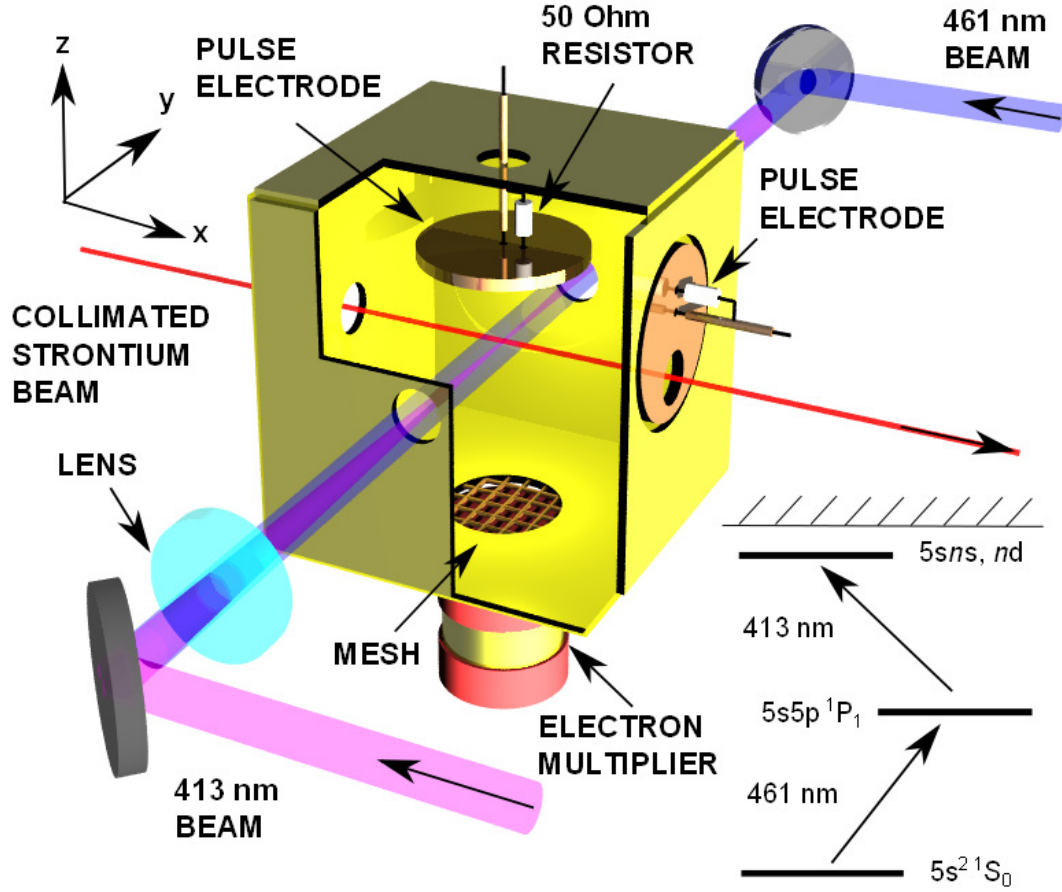


FIG. 1: (Color online) Schematic diagram of the apparatus. The inset shows the two-photon excitation scheme employed.

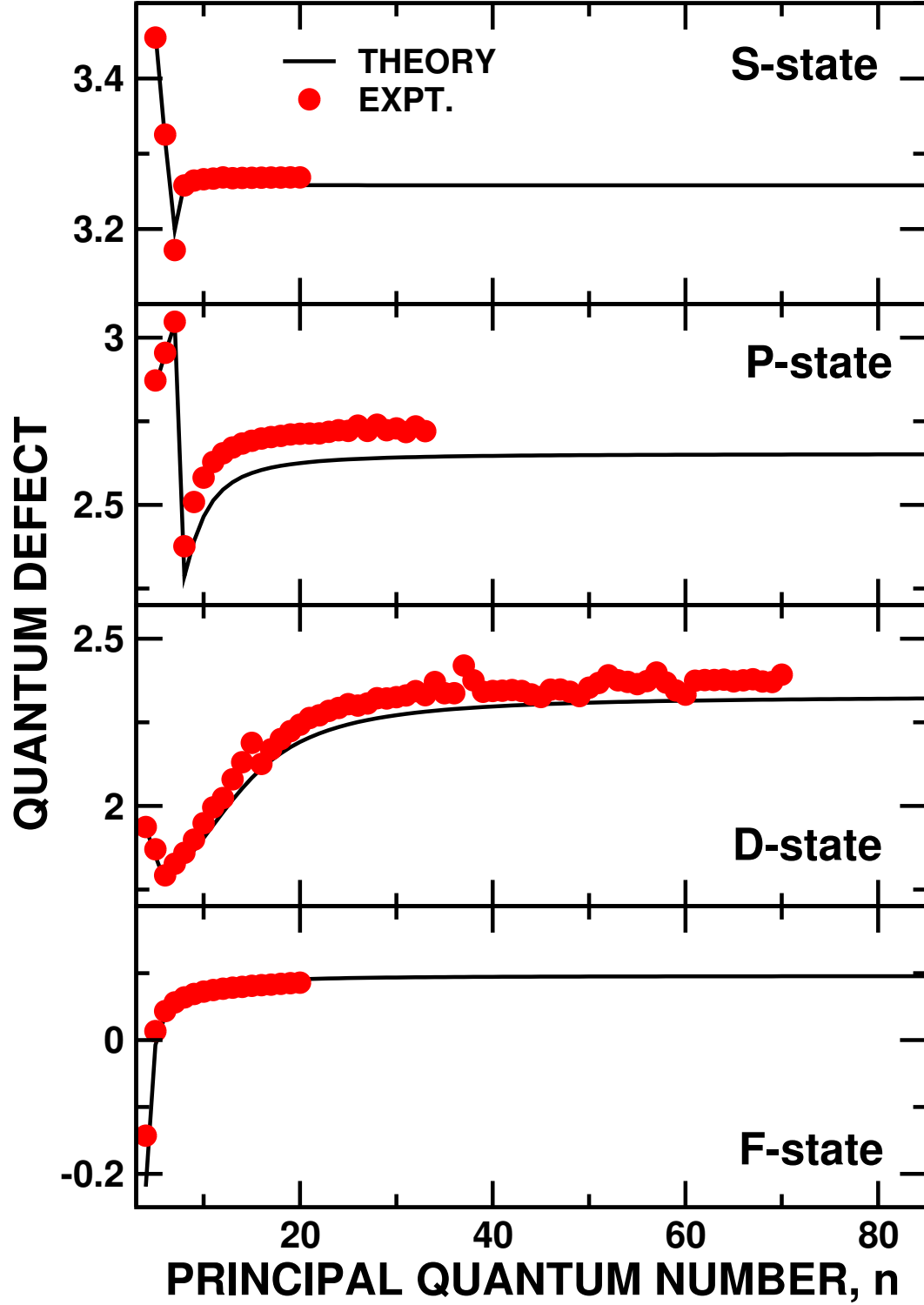


FIG. 2: (Color online) Measured and calculated quantum defects for low- $n$  Rydberg states in strontium. The calculations (solid lines) employ a two-active-electron model with six configurations (5s, 4d, 5p, 6s, 5d, and 6p) of the inner electron. Measured results (filled circles) are taken from [21] for  $n \leq 20$ , [22] for P-states ( $n > 20$ ), and [23] for D-states ( $n > 20$ ).

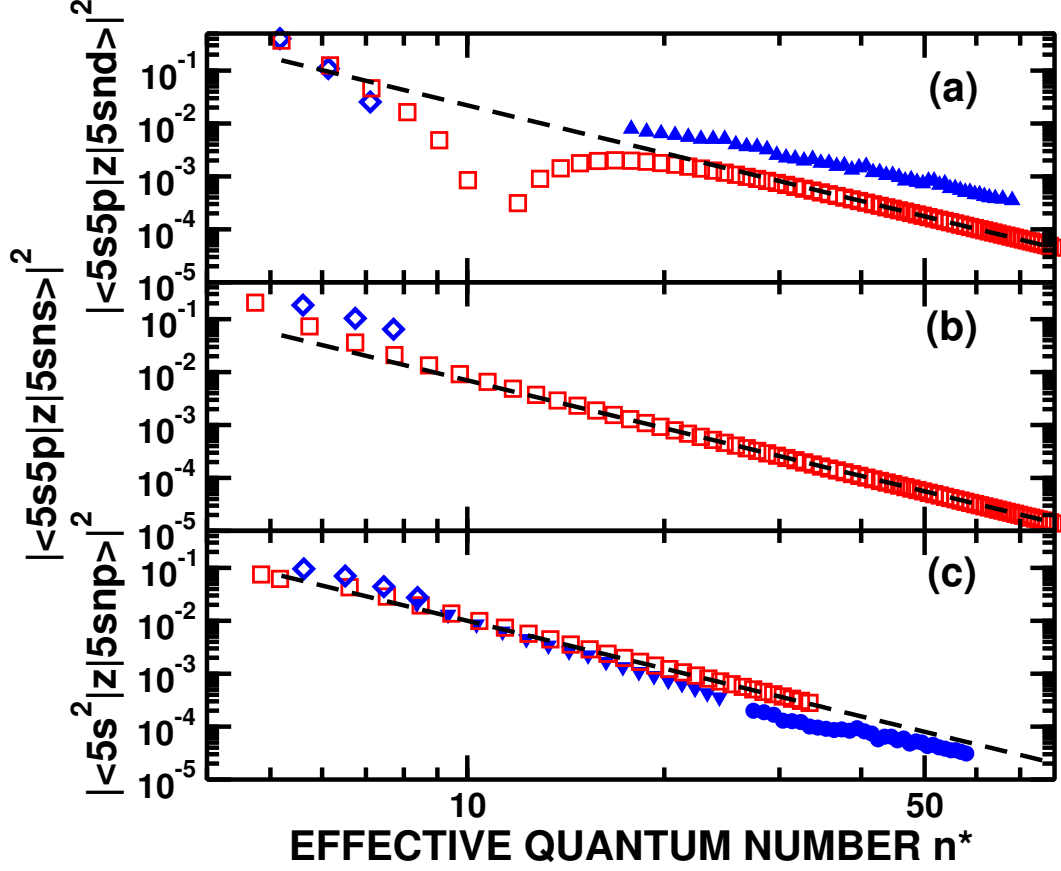


FIG. 3: (Color online) Absolute magnitude squared of the calculated dipole matrix elements (a)  $|\langle 5s5p|z|5snd\rangle|^2$ , (b)  $|\langle 5s5p|z|5sns\rangle|^2$  and (c)  $|\langle 5s^2|z|5snp\rangle|^2$  as a function of the effective principal quantum number  $n^*$ . ( $\square$  : calculations employing a TAE model with the six inner electron orbitals as in Fig. 2,  $\diamond$  : calculations from [25],  $\blacktriangle$  : measured data [26],  $\bullet$  : measured data [28], and  $\blacktriangledown$  : measured data [27].) The initial dip in (a) around  $n^* = 10$  ( $n = 13$ ) represents a Cooper minimum followed by a smooth approach to the expected  $n^{*-3}$  dependence (dashed black is drawn line to guide the eye.)

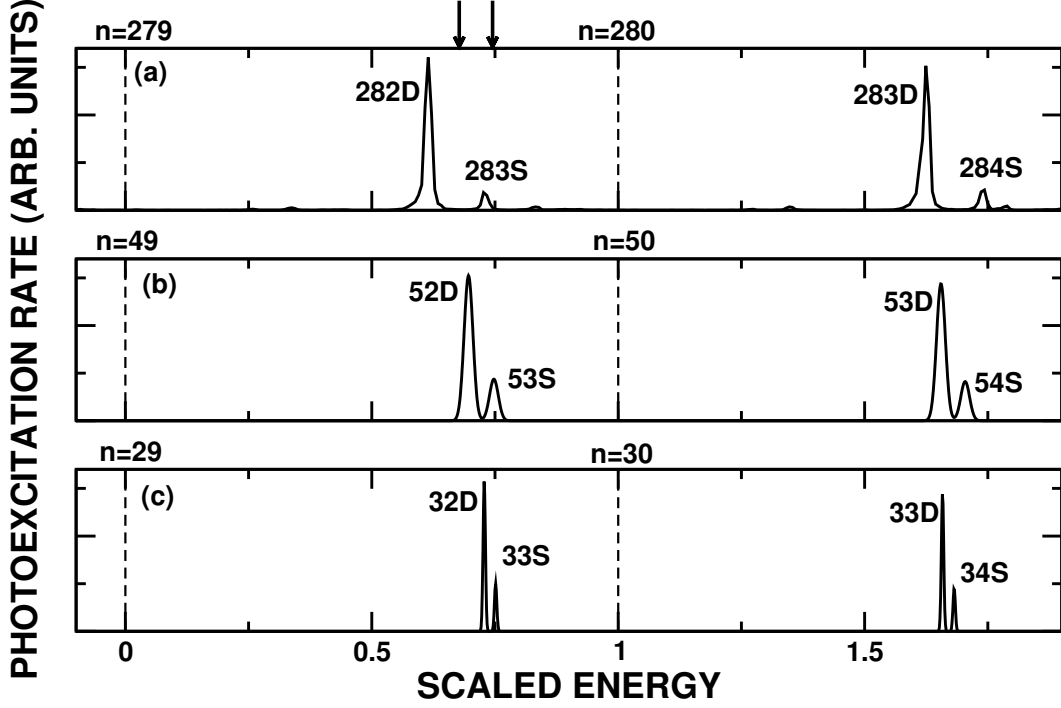


FIG. 4: Comparison between measured and calculated (zero-field) excitation spectra. (a) Measured excitation spectrum recorded at  $n \sim 283$ . (b), (c) Results of two-electron calculations at  $n \sim 50$  and  $n \sim 30$ , respectively, employing the same six inner electron states as in Fig. 2. The arrows indicate the energy for the 282d and the 283s states predicted by the scaling relations [Eqs. (7,8)] when  $\delta_\ell$  and  $\beta_\ell$  are fitted to the numerically calculated spectrum of the TAE model for  $25 \leq n \leq 85$ . To facilitate the comparison between different  $n$ , we exploit the scaling relations [Eq. (7)], a scaled energy of one corresponding to the energy difference between adjacent  $n$  and  $(n - 1)$  manifolds.

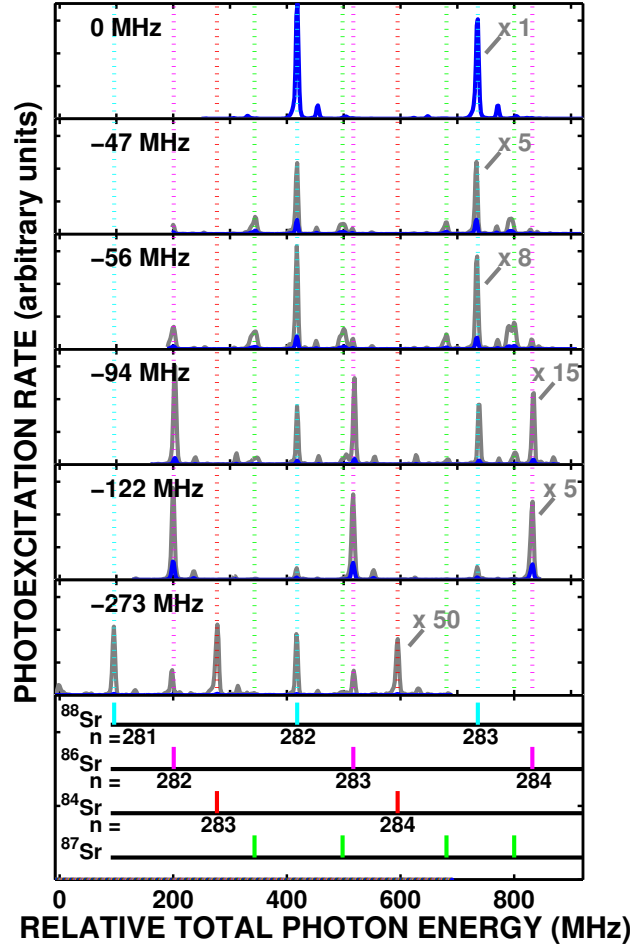


FIG. 5: (Color online) Excitation spectra recorded in the vicinity of  $n = 283$  for different detunings of the 461 nm laser. These detunings relative to the  $^{88}\text{Sr } 5s^2 \ ^1S_0 - 5s5p \ ^1P_1$  transition, are indicated (see also Table. I). Specifically, a detuning of  $\sim -122(-273)$  MHz optimizes the transition in the  $^{86}\text{Sr}$  ( $^{84}\text{Sr}$ ) isotope, while detunings of about  $-47$  and  $-56$  MHz are chosen to favor excitation of  $^{87}\text{Sr}$ . The frequency axis shows the sum of the 461 nm and 413 nm photon energies. The horizontal bars beneath the data identify the position of the  $5snd \ ^1D_2$  Rydberg states in the  $^{88}\text{Sr}$ ,  $^{86}\text{Sr}$ , and  $^{84}\text{Sr}$  isotopes, and of features attributed to excitation of  $^{87}\text{Sr}$  Rydberg states.



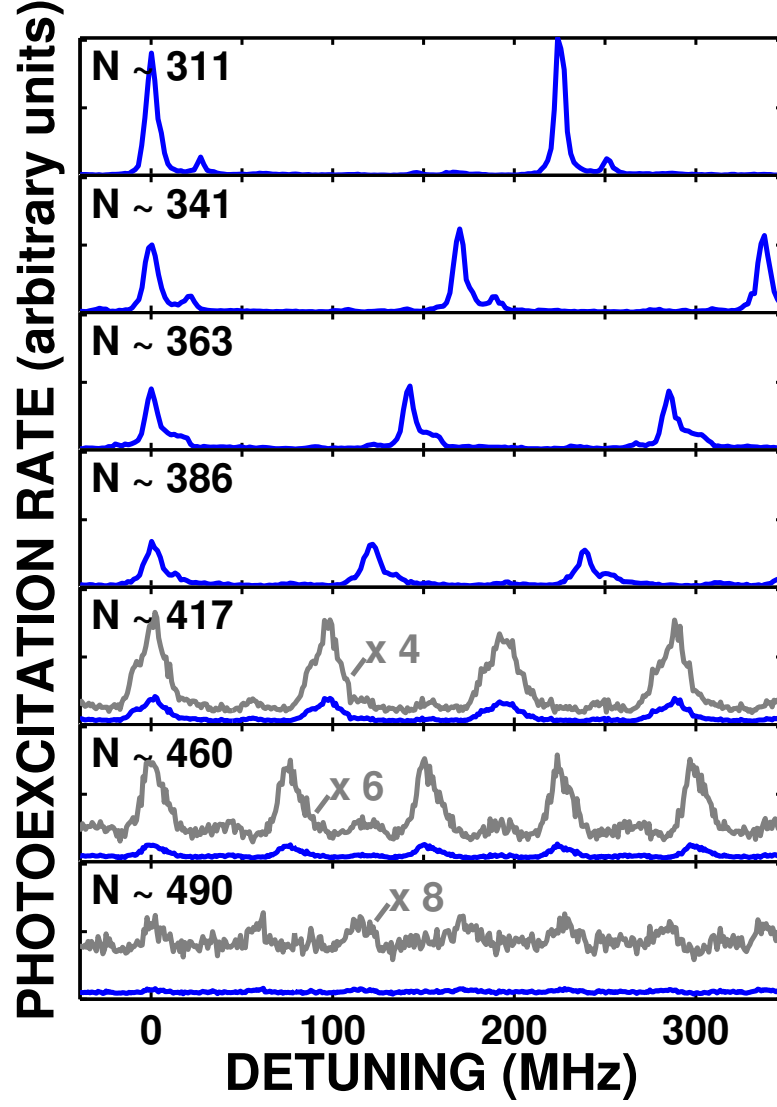


FIG. 6: (Color online) Excitation spectra recorded near the values of  $n$  indicated. The 461 nm laser is tuned to the  $^{88}\text{Sr } 5s^2 \ ^1S_0 - 5s5p \ ^1P_1$  transition. The frequency axis shows the relative frequency of the 413 nm laser during each scan.

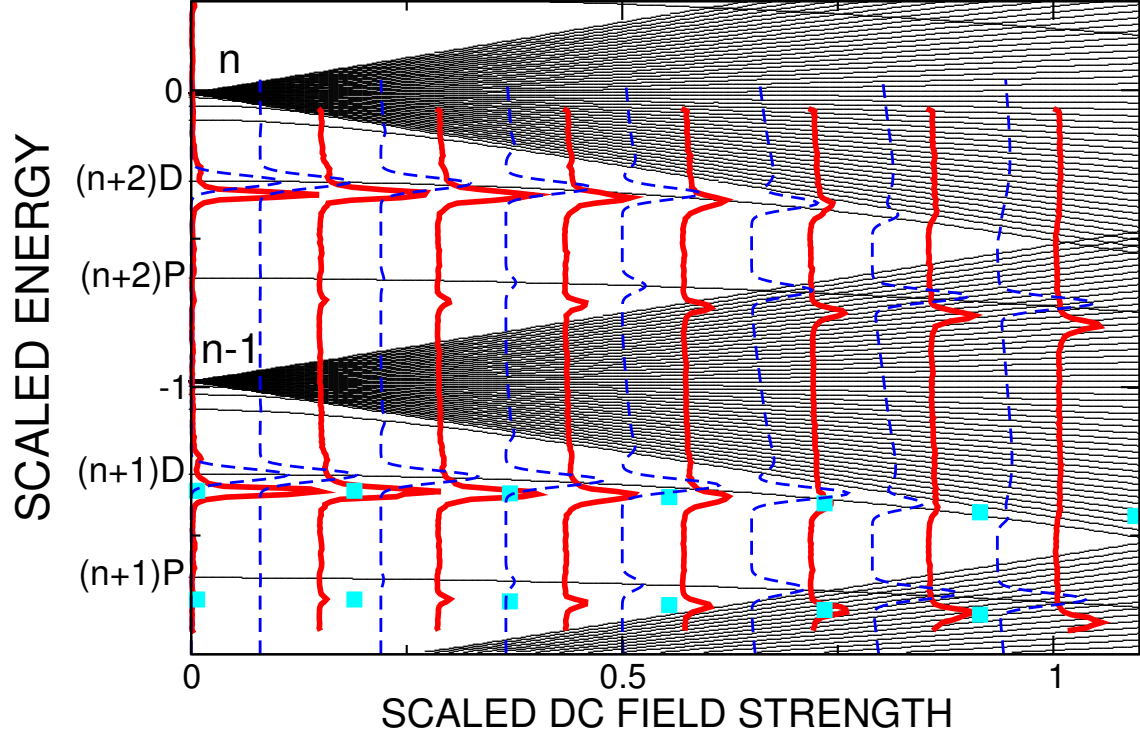


FIG. 7: (Color online) Evolution of the experimental excitation spectrum with increasing dc applied field for  $M=\pm 1$  states in the vicinity of  $n \sim 310$  (thick red line) together with the calculated eigenenergies (thin solid black lines) and the excitation spectrum (dashed blue lines) of singly-excited strontium for  $n \simeq 50$ . The squares denote the energies of earlier measurements at  $n \sim 80$  [4]. Data for the very different  $n$  levels are compared by employing scaled field and energy axes.

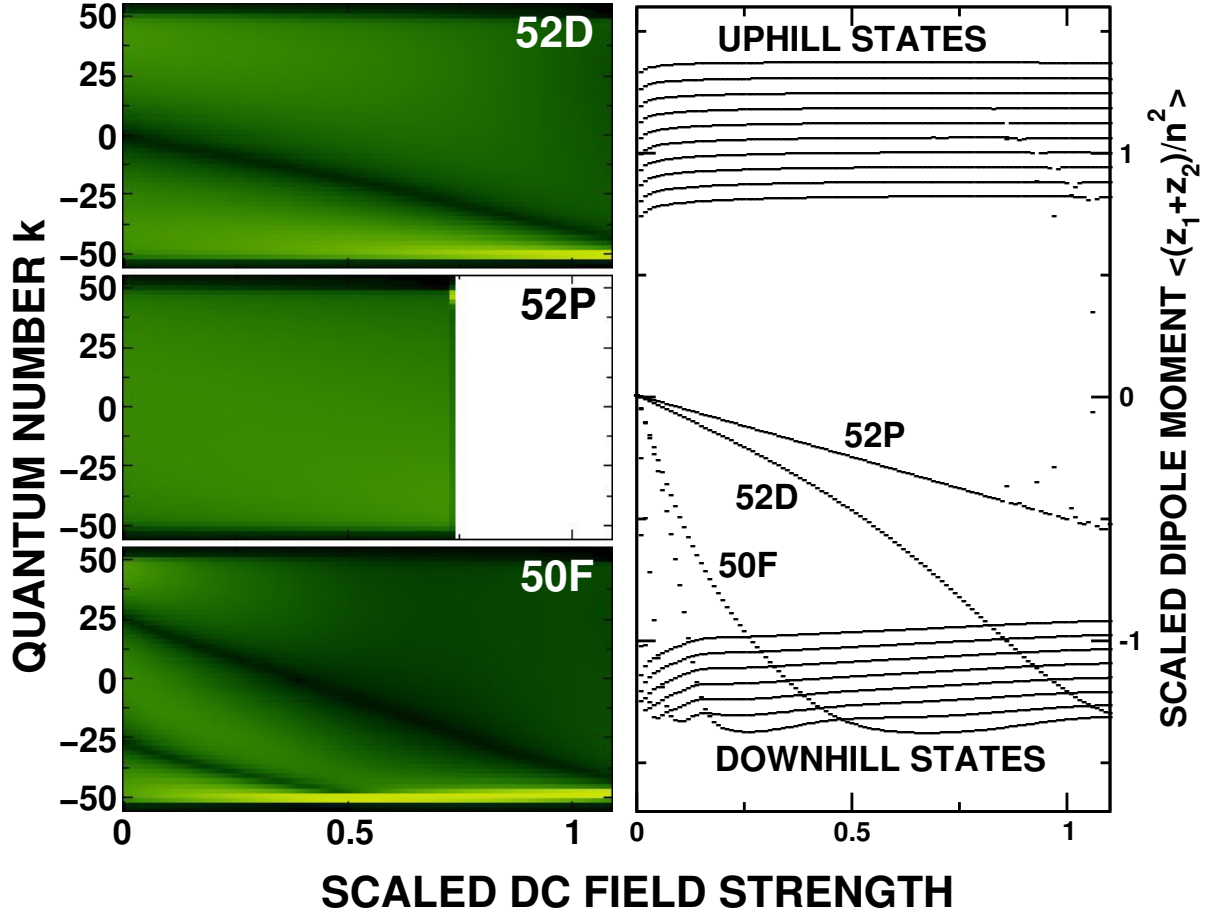


FIG. 8: (Color online) Probability distribution of the parabolic quantum number  $k$  ( $= -nA_z$ ) for the “52D”, “52P”, and “50F” states (labeled by their zero-field-designation as a function of the applied dc field  $F_{\text{dc}}$  normalized to the crossing field  $F_{\text{cross}}$  (see text). The distribution for the “52P” state is truncated where it merges with a Stark manifold. The right hand figure shows the field dependence of the average dipole moment for the same states as well as for representative extreme downhill and uphill Stark states.

## Tables

Isotope	Abundance (%)	I	F	Shift (MHz)	Relative Strength
$^{84}\text{Sr}$	0.56	0	-	-270.8	1
$^{86}\text{Sr}$	9.86	0	-	-124.5	1
$^{87}\text{Sr}$	7.00	9/2	7/2	-9.7	4/15
			9/2	-68.9	1/3
			11/2	-51.9	2/5
$^{88}\text{Sr}$	82.58	0	-	0	1

TABLE I: Properties of naturally occurring strontium. Isotope shifts and hyperfine splittings for the  $5s^2\ ^1S_0 \rightarrow 5s5p\ ^1P_1$  transitions are expressed relative to the principal  $^{88}\text{Sr}$  isotope.